High-pressure magnetic, electronic, and structural properties of $M\mathrm{Fe_2O_4}$ (M = Mg,Zn,Fe) ferric spinels

E. Greenberg,[1,*,†] W. M. Xu,[1] M. Nikolaevsky,[1,2] E. Bykova,[3] G. Garbarino,[4] K. Glazyrin,[5] D. G. Merkel,[4,‡] L. Dubrovinsky,[3] M. P. Pasternak,[1] and G. Kh. Rozenberg[1]

[1]*School of Physics and Astronomy, Tel Aviv University, 69978, Tel Aviv, Israel*

[2]*Physics Department, Nuclear Research Center Negev, Beer-Sheva 84190, Israel*

[3]*Bayerisches Geoinstitut, University of Bayreuth, Bayreuth, Germany*

[4]*European Synchrotron Radiation Facility, F-38043 Grenoble Cedex, France*

[5]*DESY, Photon Sciences, PETRA-III, P02, Notkestr. 85, Bldg. 47c, Hamburg, Germany*

(Received 21 March 2017; revised manuscript received 27 April 2017; published 23 May 2017)

Magnetic, electronic, and structural properties of $M\mathrm{Fe_2O_4}$ (M = Mg,Zn,Fe) ferric spinels have been studied by ^{57}Fe Mössbauer spectroscopy, electrical conductivity, and powder and single-crystal x-ray diffraction (XRD) to a pressure of 120 GPa and in the 2.4–300 K temperature range. These studies reveal for all materials, at the pressure range 25–40 GPa, an irreversible first-order structural transition to the postspinel $\mathrm{CaTi_2O_4}-$ type structure (*Bbmm*) in which the HS $\mathrm{Fe^{3+}}$ occupies two different crystallographic sites characterized by six- and eightfold coordination polyhedra, respectively. Above 40 GPa, an onset of a sluggish second-order high-to-low spin (HS-LS) transition is observed on the octahedral $\mathrm{Fe^{3+}}$ sites while $\mathrm{Fe^{3+}}$ occupying bicapped trigonal prism sites remain in the HS state. Despite an appreciable resistance decrease, corroborating with the transition to the LS state, $\mathrm{MgFe_2O_4}$ and $\mathrm{ZnFe_2O_4}$ remain semiconductors at this pressure range. However, in the case of $\mathrm{Fe_3O_4}$, the second-order HS-LS transition on the $\mathrm{Fe^{3+}}$ octahedral sites corroborates with a clear trend to a gap closure and formation of a semimetal state above 50 GPa. Above 65 GPa, another structural phase transition is observed in $\mathrm{Fe_3O_4}$ to a new *Pmma* structure. This transition coincides with the onset of nonmagnetic $\mathrm{Fe^{2+}}$, signifying further propagation of the gradual collapse of magnetism corroborating with a sluggish metallization process. With this, half of $\mathrm{Fe^{3+}}$ sites remain in the HS state. Thus, this paper demonstrates that, in a material with a complex crystal structure containing transition metal cation(s) in different environments, a HS-LS transition and delocalization/metallization of the 3*d* electrons does not necessarily occur simultaneously and may propagate through different crystallographic sites at different degrees of compression.

DOI: 10.1103/PhysRevB.95.195150

I. INTRODUCTION

Spinels are ternary compounds with a structure isomorphic to the mineral spinel ($\mathrm{MgAl_2O_4}$). The general formula AB_2X_4 consists of divalent X anions and most commonly cation valences of A^{2+} and B^{3+} (known as 2–3 spinels) or A^{4+} and B^{2+} (4-2 spinels). In oxide spinels, $\mathrm{O^{2-}}$ anions create a distorted cubic close-packing arrangement [1]. For 2–3 normal spinels, tetrahedral and octahedral sites are occupied by A^{2+} and B^{3+} cations, respectively. In inverse spinels, half of the B^{3+} cations occupy the tetrahedral sites, and all the A^{2+} cations occupy octahedral sites. In general, spinels can be partially inverted. Many materials can be found with the spinel structure, exhibiting a variety of electronic, magnetic, and optical properties [2–4]. A few spinels are considered gemstones, specifically transparent spinels such as $\mathrm{MgAl_2O_4}$, which is a hard mineral and has a high refraction index. Spinels are also used for industrial purposes, due to their hardness and stability upon exposure to high temperatures, chemicals, and physical wear [5].

The spinel structure and its high-pressure (HP) modification, the so called postspinel, are adopted by many minerals and compounds which play an important role in modeling the properties and geochemistry of Earth's transition zone and mantle. Therefore, the behavior of spinels under nonambient conditions is of considerable geophysical importance and has been the subject of several powder x-ray diffraction (XRD) studies [6–10]. These studies performed for $\mathrm{MgFe_2O_4}$, $\mathrm{MgAl_2O_4}$, and $\mathrm{ZnFe_2O_4}$ have shown a pressure-induced first-order structural transition to more compact postspinel structures [6–10] in the pressure range 25–45 GPa. However, there is controversy regarding the ascertainment of the postspinel structure(s), with the most commonly given candidates being $\mathrm{CaMn_2O_4}$, $\mathrm{CaTi_2O_4}$, and $\mathrm{CaFe_2O_4}$ type structures. These three structure types are orthorhombic and have the $\mathrm{Ca^{2+}}$ in a bicapped trigonal prism coordination (eight surrounding $\mathrm{O^{2-}}$) and the transition metal in octahedral coordination. The main difference between the three structures, besides the difference in symmetry, is that $\mathrm{CaFe_2O_4}$ contains two different crystallographic sites for $\mathrm{Fe^{3+}}$, whereas in the other structures, all the octahedra are equivalent.

Previous studies of an archetypal spinel and the oldest recognized natural magnetic material, magnetite ($\mathrm{Fe^{2+}Fe^{3+}{}_2O_4}$), utilizing ^{57}Fe Mössbauer spectroscopy (MS), also revealed a pressure-induced first-order phase transition at the pressure range 25–45 GPa [11], in good agreement with XRD studies [12–14]. However, according to MS measurements [11], the

*erangre@gmail.com

†Present address: Center for Advanced Radiation Sources, University of Chicago, Argonne Illinois 60439, USA.

‡On leave from Institute for Particle and Nuclear Physics, Wigner Research Centre for Physics, Hungarian Academy of Sciences, H-1525 Budapest, Hungary.

postspinel phase exhibits, in addition to the Fe^{2+} site, two distinct Fe^{3+} sites with different hyperfine interaction parameters. These MS results appear inconsistent with the abovementioned XRD studies claiming that the postspinel Fe_3O_4 phase is of the $CaMn_2O_4$ or $CaTi_2O_4$ type structures, wherein all Fe^{3+} cations should occupy equivalent crystallographic sites. The possible incongruity between the structure modeled from XRD data and the MS data can be attributed to the lack of necessary resolution due to the intrinsic broad lines of the HP XRD powder data, which may not provide sufficient information for a reliable structure assignment. Precise single-crystal XRD could be crucial in such a case for the final structural assignment within the postspinel pressure range.

The MS and electrical resistance $R(P,T)$ studies of magnetite also revealed another important result—the absence at the pressure range up to 120 GPa of any *first-order* pressure-induced electronic transformations typical for Fe^{3+}, namely, Mott or high-to-low spin (HS-LS) transition. Such electronic transitions are usually observed at the pressure range of 40–60 GPa and typically coincide with a first-order structural phase transition [15,16]. In the meantime, only a partial sluggish magnetic $\rightarrow$ nonmagnetic transition was observed at the range 40–80 GPa, though most of the iron remains in a high-spin state. Thus, the feature observed in Fe_3O_4 is drastically different from the behavior of all other previously studied ferric compounds, therefore requiring further thorough studies and analysis. However, since magnetite contains both Fe^{2+} and Fe^{3+}, with Fe^{3+} occupying two different sites, the resulting MS spectra are rather complicated, and a high-quality analysis of the MS data is quite difficult. Comparative studies of different ferric spinels, with Fe^{2+} substituted by another M^{2+} cation, can simplify the analysis of the HP behavior of the postspinel phase. The main objectives of this paper are detailed and accurate combined single-crystal and powder XRD, ^{57}Fe MS and electrical resistance studies of the typical normal and inverse $M^{2+}Fe^{3+}{}_2O_4$(M = Mg,Zn,Fe) ferric spinels in a wide pressure range, focusing on $P > 40$GPa, in order to resolve the dilemma of the postspinel structure of ferric spinels (particularly of magnetite), and to clarify the nature of their unusual electronic behavior under pressure.

II. EXPERIMENTAL

Samples of MFe_2O_4 (M = Mg,Zn) were prepared by a solid-state reaction of MgO and ZnO with Fe_2O_3 at high temperatures, as already described [17]. The single-crystal experiments were performed with a sample of $MgFe_2O_4$ and a natural single-crystal sample of magnetite.

Custom 4-pin diamond anvil cells (DACs) made at Bayerisches Geoinstitut and Tel-Aviv University [18], and European Synchrotron Radiation Facility (ESRF) membrane cells [19] along with diamond anvils with culet diameters of 150–320 μm were used to induce high pressure. Re or stainless steel gaskets were pressed to a thickness of 15–30 μm, and the sample was placed in a cavity of 70–120 μm diameter. It should be noted that different pressure transmitting media were used for the different measurement techniques. X-ray diffraction measurements were performed using pressurized Ne or He gas, whereas Mössbauer spectra were collected mainly using cryogenically loaded N_2. For the resistance measurements, the mixture of Al_2O_3 − NaCl was used both as an insulating layer and a pressure medium. Along with the samples, small spheres of ruby were added for pressure measurement using the ruby R_1-line fluorescence spectroscopy [20–22]. For $ZnFe_2O_4$, XRD data of a small Au strip was used for manometry [23].

Mössbauer spectroscopy measurements were performed using a nominal 10 mCi ^{57}Co(Rh) point source. Either Wissoft software (WissEl GmbH) or Maestro and MCS-Plus (EG&G Ortec) were used to set the 14.4 keV gate and collect the transmission data from the proportional counter. Low-temperature MS was performed using a custom made top-loading liquid nitrogen/liquid helium cryostat. The typical collection time for each spectrum was ∼24 h. A limited number of spectra for $ZnFe_2O_4$ and Fe_3O_4 were collected using synchrotron energy-domain Mössbauer measurement (SMS) carried out at beamline ID18 at ESRF at temperatures down to 2.4 K (see [24] for more details). These spectra were collected with the source at room temperature and, therefore, are affected by the second-order Doppler shift. The spectra for Fe_3O_4 were collected at ID18 for the same sample which was used for powder XRD studies using He pressure medium. Fitting of the spectra was performed by means of the least-squares method [25] from which the following MS parameters were obtained: relative abundance of the Fe spectral components, the isomer shift (IS), the quadrupole splitting, the hyperfine field, the line-width and an area asymmetry parameter. The reported velocity is with respect to α-Fe at room temperature. The $ZnFe_2O_4$ and $MgFe_2O_4$ samples used for MS studies were enriched with 25% ^{57}Fe.

Powder XRD measurements were carried out at room temperature in angle-dispersive mode with wavelengths of 0.3738 and 0.4152 Å at ESRF, Grenoble, at the ID27 and ID09 beam lines, respectively. Diffraction images were collected using a MAR CCD detector. The image data were integrated using FIT2D [26,27] and DIOPTAS [28], and the resulting diffraction patterns were analyzed with the GSAS+EXPGUI [29,30] program.

Single-crystal synchrotron XRD experiments have been performed at the Extreme Conditions Beamline (ECB), P02.2, at PETRA III, Hamburg, Germany [31]. Diffraction images were collected using a Perkin Elmer flat panel detector. In the experiment with Fe_3O_4, the energy of the synchrotron radiation was set to 42.72 keV($\lambda = 0.29023$ Å), and the x-ray beam was focused down to $3.0(V) \times 8.0(H)\,\mu m^2$ with compound reflective lenses. The single crystal of Fe_3O_4 was compressed from 3 to 51 GPa with a 2 to 5 GPa step. In the experiment with $MgFe_2O_4$, the synchrotron x-ray beam (42.81 keV, $\lambda = 0.28962$ Å) was focused down to $2.4(V) \times 4.0(H)\,\mu m^2$ using Kirkpatrick-Baez mirrors. The XRD data were collected at four pressure points (2.6, 14.6, 28.4, and 34.4 GPa).

In both experiments, at every pressure step, we collected XRD images during continuous rotation of DACs typically from −25 to +25 on omega. FIT2D [26,27] software was used to analyze the 2D images. CeO_2 standard (SRM 674b) from the National Institute of Standards and Technology was used to calibrate coordinates of the beam center, tilt angle, and tilt plane rotation angle. At selected pressure points, data collection experiments were performed by narrow 0.5-1° omega-scanning in the range from −40° to +40°. Integration of the reflection intensities and absorption corrections

were performed using CrysAlisPro software [32]. A single crystal of an orthoenstatite $[(Mg_{1.93},Fe_{0.06})(Si_{1.93},Al_{0.06})O_6$, $Pbca$, $a = 8.8117(2)$, $b = 5.18320(10)$, $c = 18.2391(3)$ Å] was used to calibrate the instrument model of CrysAlisPro software (sample-to-detector distance, the detector's origin, offsets of the goniometer angles, and rotation of the x-ray beam and the detector around the instrument axis). The structures were solved by the direct method and refined by full matrix least-squares using SHELXTL software [33].

For *resistance measurements*, the Re gaskets were covered with a layer of $Al_2O_3 - NaCl$ (3:1 wt. %) mixed with epoxy. Conducting wires were connected to small triangular shaped Pt foils, leading from the base of the diamond to the center of the culet, using a conductive epoxy. For low-temperature measurements, each DAC was placed on a probe connected to a step motor, which slowly lowers the DAC into a N_2 or He Dewar. The temperature was monitored by a Lakeshore DT-421-HR diode. Resistance was measured by applying various currents on the sample and measuring the resulting voltages. At each temperature, ~30 different currents were applied to the sample with the measured temperature varying by less than 0.3 K for the whole duration.

III. RESULTS

A. MS

1. $MgFe_2O_4$ and $ZnFe_2O_4$

Mössbauer spectroscopy measurements of $MgFe_2O_4$ and $ZnFe_2O_4$ were performed up to ~110 and ~88 GPa, respectively. At ambient conditions, the Mössbauer spectrum of $MgFe_2O_4$ consists of two sextets corresponding to two low-pressure (LP) Fe^{3+} structural sites (inverse spinel), tetrahedral and octahedral [Fig. 1(a)]. Both spectral components have almost equal spectral intensity with similar IS values of 0.41(2) mm/s. The two components exhibit different magnetic hyperfine fields $H_{hf} = 50.2(0.32)$ and 52.5(0.32) T at 90 K, typical for a ferric-oxide high-spin $^6A_{1g}$ state in tetrahedral and octahedral environments. Between ambient pressure and 20 GPa, the observed spectra barely change with the only observable variation being a slight decrease in IS [see Figs. 1(a) and 2(a)] and about 3% increase in H_{hf}. In the case of $ZnFe_2O_4$, the Mössbauer spectrum at ambient conditions [Fig. 1(b)] consists of only one doublet, corresponding to Fe^{3+} octahedral sites (normal spinel) with IS = 0.342(6)mm/s and quadrupole splitting QS = 0.425(7)mm/s. As a result of a weak magnetic coupling, $ZnFe_2O_4$ has a relatively low ordering temperature $T_N = 10.5$ K at ambient pressure [34]. Similar to $MgFe_2O_4$, the spectra barely change with pressure up to 24 GPa [Figs. 1(b) and 2(b)].

At the pressure range 25–40 GPa for both studied materials, a significant change occurs in the MS spectra; namely, the appearance of two new paramagnetic components, and above 40 GPa, the only components remaining are these paramagnetic components. These two new components, designated as PS1 and PS2, are characterized by quite different QS and IS values (Fig. 2). It is noteworthy, that the IS values for the PS1 and LP components are pretty close, suggesting the same nearest-neighbor environment; namely, an octahedral configuration. Low-temperature measurements (Fig. 3) show

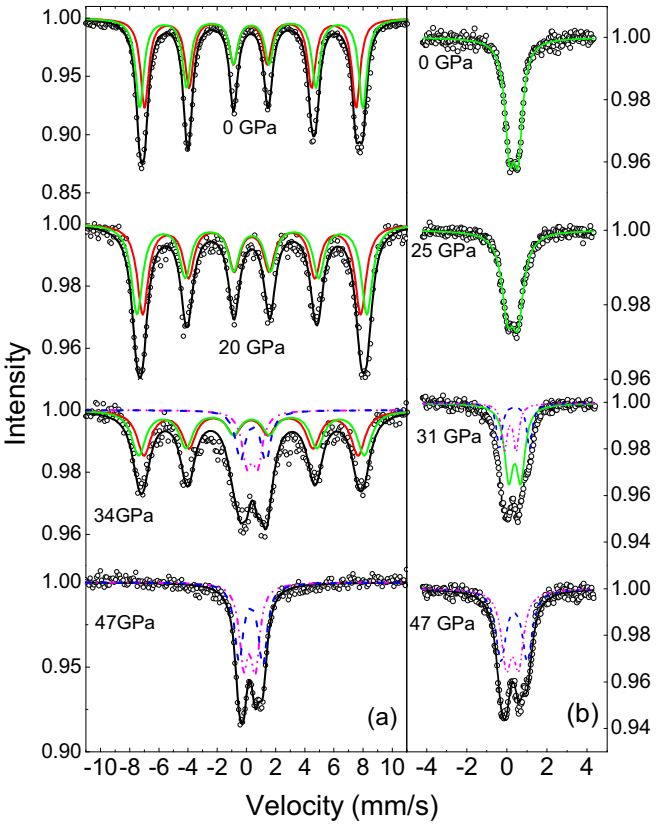

FIG. 1. Mössbauer spectra of (a) $MgFe_2O_4$ and (b) $ZnFe_2O_4$ recorded at room temperature and various pressures. For $MgFe_2O_4$, two Fe^{3+} components at the spinel phase correspond to the tetrahedral and octahedral sites. At 29 GPa, two paramagnetic components appear in the central part of the spectrum. The abundance of the new phase increases with pressure, reaching 100% above 40 GPa. For $ZnFe_2O_4$, the spectra up to 24 GPa consist of only one doublet, corresponding to Fe^{3+} in the spinel octahedral sites. Above 25 GPa, two new Fe^{3+} sites appear (dashed and dash-dot-dotted lines) corresponding to the components of the HP phase.

that these new components are magnetically split with a Néel temperature of $T_N \approx 90$ K (47 GPa) for both materials. The magnetic hyperfine fields $H_{hf} = 42.4(3)$ and 46.9(4) T for $MgFe_2O_4$ at 50 K, typical of a Fe^{3+} HS state with a more covalent nature. Similar H_{hf} values, 40.3(5) and 46.4(3) T at 80 K, were obtained for $ZnFe_2O_4$.

It is noteworthy that, with the formation of the postspinel phase, the chain of transformations is not finished yet. Low-temperature measurements show that, with further pressure increase above 50 GPa, an appearance of a new broad component (Fig. 4), designated as PS3, is observed in the central part of the spectra, characterized by the significantly reduced IS value of ~0.12 and ~0.17 mm/s for $MgFe_2O_4$ and $ZnFe_2O_4$, respectively (Fig. 2). The abundance of the new component increases sluggishly, replacing the PS1 component [see inset Fig. 5(a)]. The temperature dependences of the Mössbauer spectra at 80 GPa for $MgFe_2O_4$ and 88 GPa for $ZnFe_2O_4$ are shown in Fig. 4. Low-temperature measurements show the gradual broadening of the absorption spectrum and the increase of QS with the decrease in temperature. Below 50 K, the onset of a magnetic splitting corresponding with the ordering of

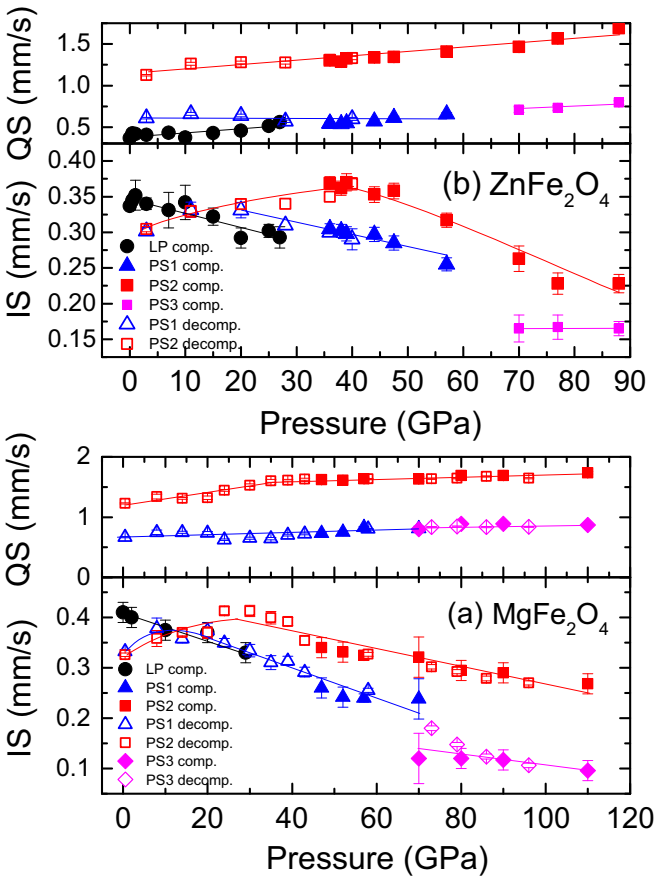

FIG. 2. The pressure evolution of the IS and the quadrupole splitting of (a) $MgFe_2O_4$ and (b) $ZnFe_2O_4$ at 300 K relative to a ^{57}Co(Rh) source at 300 K. Note that, above 60 GPa, the PS1 component is replaced by the PS3 component characterized by a significantly reduced IS value. All lines are to guide the eye. Symbols: "●" represents the spinel, "▲" and "■" the PS1 and PS2 components, respectively, "◆" the PS3 component. Filled and empty shapes mark compression and decompression cycles, respectively. The pressure uncertainties are 5%.

the HS PS2 component appears, and below 8 K, one clearly observes the onset of a smeared magnetic splitting corresponding with the PS3 component, which are obvious features of a paramagnetic spin relaxation phenomenon (see [35]).

Mössbauer spectra obtained at room temperature during decompression showed a significant hysteresis at the pressure range below 40 GPa, suggesting that the transition to the postspinel phase is not reversible or strongly suppressed by the effect of kinetics. With reducing pressure, only the components of the postspinel phase are observed down to ambient pressure (Fig. 2, and Fig. S1 in the Supplemental Material [36]). Contrarily, no hysteresis was observed in the IS(P) behavior at the range 50–70 GPa, suggesting a fully reversible transformation at this pressure range.

2. Fe_3O_4

In the case of magnetite Fe_3O_4, the performed low-temperature MS studies show a similar evolution of the MS spectra at the pressure range 45–80 GPa. It is noteworthy that the Fe_3O_4 postspinel phase, at its appearance, is characterized by three equally abundant Fe HS components [Fe^{2+},Fe^{3+}(I),Fe^{3+}(II)] [11]. At pressures above 40 GPa, similar to $MgFe_2O_4$ and $ZnFe_2O_4$, a new quadrupole-split component, characterized by the significantly reduced IS value of ~0.16mm/s, emerges at the center of the spectra (Fig. 6). This component was designated as $Fe^{3+}(I)_{nm}$. Its abundance increases gradually with pressure at the expense of the Fe^{3+}(I) HS component, reaching 1/3 value at ~80 GPa when the latter component completely disappears (Fig. 6). However, in contrast to $MgFe_2O_4$ and $ZnFe_2O_4$, in Fe_3O_4, the electronic transition is not finished yet with the completion of this transformation. Above 70 GPa, another nonsplit component appears at the center of the spectra, with its abundance increasing gradually at the expense of the Fe^{2+} component (Fig. 6). This component was designated as $Fe^{2+}{}_{nm}$. The onset of these new components coincides with the decrease of the magnetic ordering temperature of the HS magnetically split components from 380 K at 55 GPa to 160 K at 82 GPa [11]. It is noteworthy that, in the case of using N_2 pressure medium, part of the Fe^{2+} ions remain in the HS state even at 120 GPa (Fig. 6). Meanwhile, using He as pressure medium results in a complete transformation on Fe^{2+} sites even at about 84 GPa (Fig. 7). We suggest that these observations highlight the sensitivity of the electronic transition to additional stresses and deviation from quasihydrostatic conditions. Low-temperature measurements show no sign of broadening or splitting of the absorption spectrum and no increase of QS for $Fe^{2+}{}_{nm}$ and $Fe^{3+}(I)_{nm}$ components with the decrease in temperature down to 2.4 K, which means no features of a magnetic interaction.

B. XRD

Powder XRD measurements of $MgFe_2O_4$, $ZnFe_2O_4$, and Fe_3O_4 were carried out up to 53, 70, and 120 GPa, respectively. Consistent with MS, our XRD studies show an irreversible first-order structural transition at the range 25–40 GPa in each of the spinels. Particularly, the coexistence range of the LP and HP phases for $MgFe_2O_4$, $ZnFe_2O_4$, and Fe_3O_4 is 30–42 GPa, 25–36 GPa, and 28–40, respectively. Based on the MS studies, our initial interpretation was that the HP postspinel phases of MFe_2O_4 ferrite spinels are not of the $CaMn_2O_4$ (*Pbcm*) or $CaTi_2O_4$ (*Bbmm*) structure types. The only structure from the earlier proposed models, characterized by two different Fe^{3+} sites, is the $CaFe_2O_4$ (*Pnma*) type. Fitting using this structural model gives rather good results in the case of F(calc) weighted (model biased Le Bail) refinement, but poor results in the case of a full-profile Rietveld refinement, which takes into account the atomic positions. Another possibility which should be considered is that, within these structure types, some of the Fe^{3+} cations exchange positions with M^{2+} cations, similar to the inversion within the original spinel structure. In such a case, $CaMn_2O_4$- or $CaTi_2O_4$-type structures could be also consistent with the obtained MS results. Indeed, Rietveld refinement of $MgFe_2O_4$, $ZnFe_2O_4$, and Fe_3O_4 [37] powder diffraction data, assuming the $CaTi_2O_4$-type structure with the Fe^{3+} occupying two different crystallographic sites, results in a reasonable fit to the data, as evidenced in Figs. 8(a)–8(c) (background subtracted quality factors: $w_{Rp} < 0.45\%, Rp < 0.32\%, w_{Rp} < 1.4\%, Rp < 0.96\%$, and $w_{Rp} < 2.3\%, Rp < 1.3\%$, respectively). However, a fit to $CaMn_2O_4$-type structure

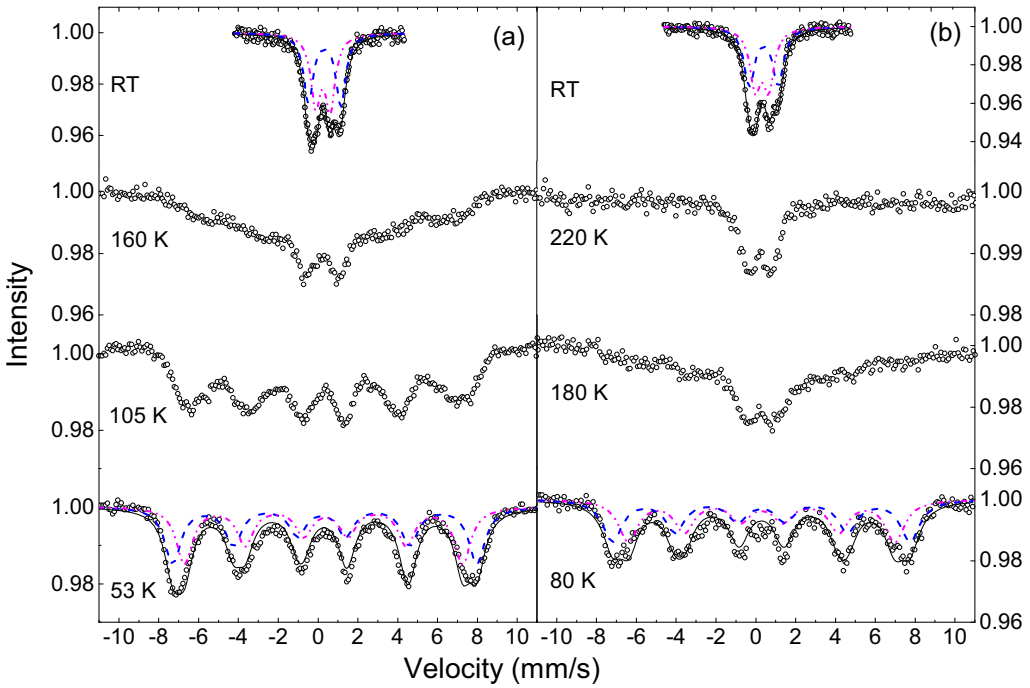

FIG. 3. Mössbauer spectra of (a) $MgFe_2O_4$ and (b) $ZnFe_2O_4$ recorded at 47 GPa and various temperatures; spectra were fit with two Fe^{3+} sites PS2 and PS1 (dashed and dash-dot-dotted lines, respectively). A strong magnetic relaxation effect is observed below 200 K, and below 100 K, the hyperfine fields become saturated. Note a slight discrepancy between the experimental and calculated data at the central part of the spectra at 53 and 80 K.

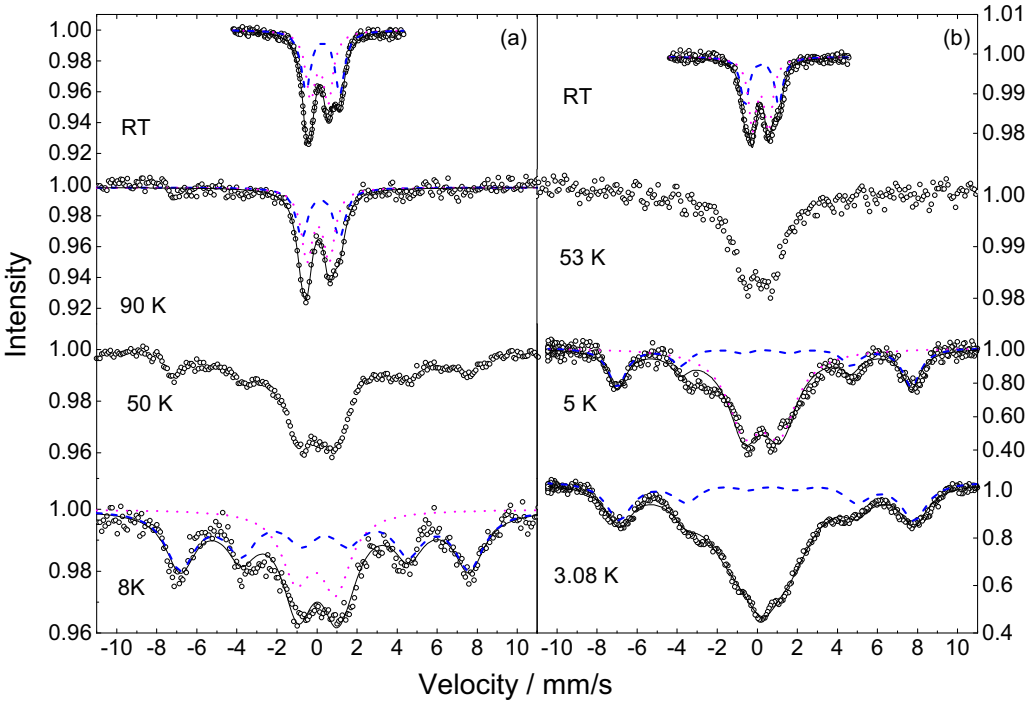

FIG. 4. Mössbauer spectra of (a) $MgFe_2O_4$ and (b) $ZnFe_2O_4$ recorded at 80 and 88 GPa, respectively, and various temperatures. The spectra below 50 K are characterized by the two components: the first is characterized by a static magnetic hyperfine interaction $H_{hf} = 45$ T (HS PS2 component, dashed line), and the second by a spin-spin magnetic relaxation spectrum (PS3 component, dotted line), the typical feature of the LS state [31]. Note that the magnetic ordering temperature for the HS component drops from ~100 K at 47 GPa (Fig. 3) to below 50 K here. The spectra of $ZnFe_2O_4$ at 84 GPa, 5 and 3.08 K were collected using energy-domain MS carried out at the beamline ID18 at ESRF.

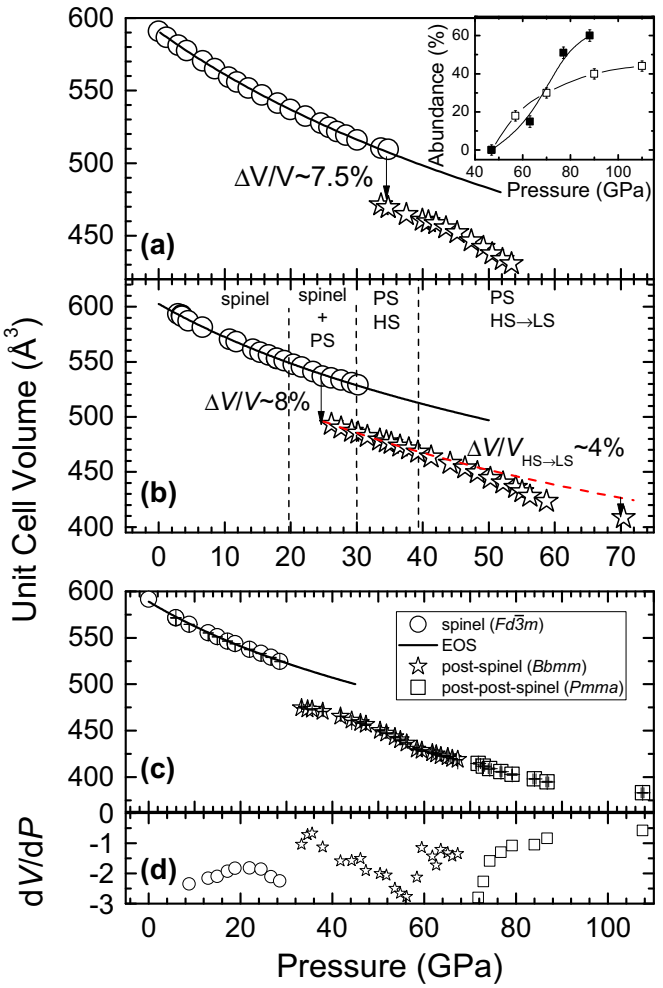

FIG. 5. Unit-cell volume of the spinel and postspinel $CaTi_2O_4$-type phases of (a) $MgFe_2O_4$, (b) $ZnFe_2O_4$, and (c) Fe_3O_4 as a function of pressure at room temperature; (d) pressure derivative of the unit-cell volume for Fe_3O_4 as a function of pressure. Circles ○ and stars ☆ represent the spinel and postspinel phases, respectively. The solid lines are fits to the second-order Birch-Murnaghan EOS of the spinel phases extrapolated to ∼50 GPa, fitting results in the values of $K_0 =$ 170.5(8),174.1(2) [17], 198(9) GPa, and $V_0 = 591.0(2)$,602.8(4), and 589.0(2) Å^3 for $M =$ Mg,Zn, and Fe, respectively. The third-order EOS for Fe_3O_4 results in $V_0 = 590(3)$ Å^3, $K_0 = 182(29)$ GPa, and $K' = 5(2)$. The dashed line represents a fit to the postspinel phase of $ZnFe_2O_4$ at the pressure range 25–40 GPa. Note a steeper decrease of unit-cell volume with pressure increase above 40 GPa, indicating a HS-LS transition on the octahedral sites. The inset shows the abundance of the quadrupole-split paramagnetic MS component as a function of pressure in $MgFe_2O_4$ and $ZnFe_2O_4$ (open and solid squares, respectively).

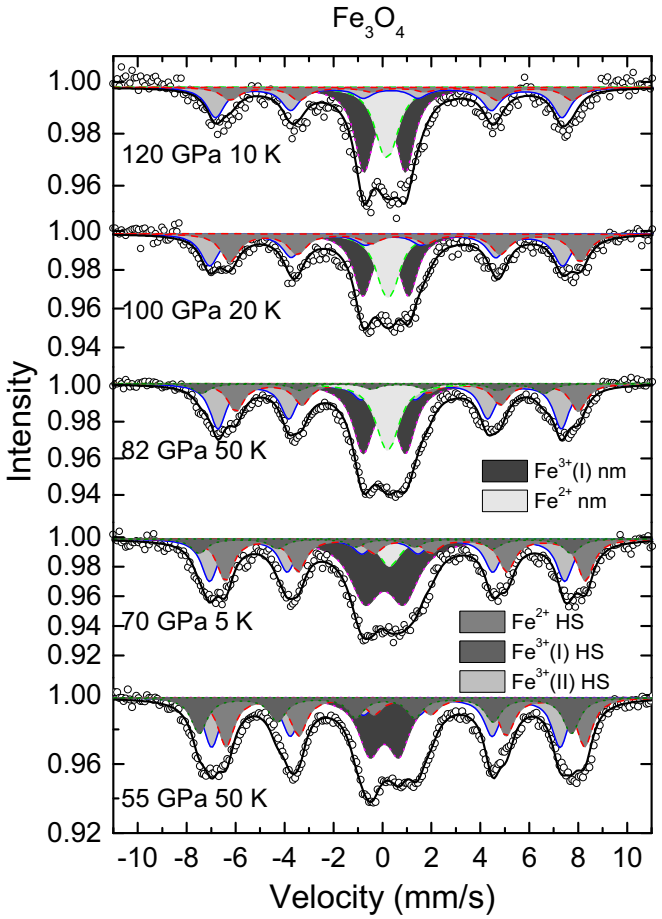

FIG. 6. Mössbauer spectra of Fe_3O_4 recorded at various pressures and low temperatures (N_2 pressure medium). Note that, at its appearance, the postspinel phase is characterized by three equally abundant Fe components [14] [Fe^{2+},Fe^{3+}(I),Fe^{3+}(II): red dashed, olive dotted, and blue solid lines, respectively]. Above 40 GPa, an onset of a new quadrupole-split Fe^{3+}(I)$_{nm}$ component is observed (magenta dotted line), replacing the Fe^{3+}(I) component. Around 70 GPa, another unsplit Fe$^{2+}_{nm}$ component appears (green dashed line), gradually replacing the Fe^{2+} component. Components are shaded for grayscale viewing offline.

with the Fe^{3+} occupying two different crystallographic sites is also possible, with rather similar results.

To resolve this problem and to get a final structure assignment, we have performed single-crystal XRD studies of $MgFe_2O_4$ and Fe_3O_4. For both materials, the HP phase has been identified as belonging to the *Bbmm* (or equivalent *Cmcm*) space group (Fig. 9). The complete details of the single-crystal refinement for $MgFe_2O_4$ at 27.4(5) GPa and Fe_3O_4 at 28.4(5) GPa are given in Table I and Supplemental Table 1 [36], respectively. The obtained unit-cell volumes are similar to those obtained in previous experiments [10,38] reporting either the $CaTi_2O_4$ or $CaMn_2O_4$ structures and similar to our powder XRD data. However, since the single-crystal refinement is free from additional effects such as texture, compared to powder diffraction refinement, we are able to more accurately determine the atomic positions and site occupancy of the different cations. Table II shows the atomic positions and site occupancies of the Fe^{3+}, Mg^{2+}, and O^{2-} ions of $MgFe_2O_4$. Thus, from single-crystal refinement, we determine that the Fe^{3+} cations do not occupy solely the octahedral $8f$ Wyckoff sites; there is in fact a partial inversion with the Mg^{2+} cations: about 64% of Fe^{3+} ions occupy octahedral sites, while the rest are in bicapped trigonal prism. For the Fe_3O_4 sample (see Supplemental Table 2 [36]), we cannot determine whether there is any inversion because

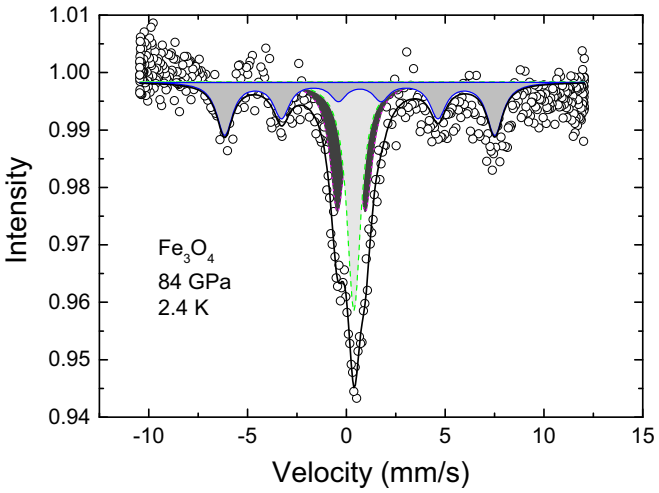

FIG. 7. The spectra of Fe_3O_4 at 84 GPa and 2.4 K collected using energy-domain MS (He pressure medium). Note that only three equal abundant components are observed at this pressure, namely $Fe^{2+}{}_{nm}$, $Fe^{3+}(I)_{nm}$, and $Fe^{3+}(II)$. This suggests that using the He pressure medium results in a complete electronic transformation on the octahedral sites at about 84 GPa. Meanwhile, Fe^{3+} ions occupying square antiprism coordinated sites remain in the HS state (blue solid line). The lack of any sign of a magnetic interaction for $Fe^{2+}{}_{nm}$ and $Fe^{3+}(I)_{nm}$ components (green dashed and magenta dotted lines, respectively) above 84 GPa and down to 2.4 K suggests that these components emanate not from a paramagnetic, but rather from a nonmagnetic state. Components are shaded for grayscale viewing offline.

it is not possible to distinguish between Fe^{2+} and Fe^{3+} with single-crystal diffraction. As expected, the transition from a structure with four- and sixfold coordination to a structure with six- and eightfold coordination results in an increase in the average ⟨Fe-O⟩ distances. Within the spinel phase of $MgFe_2O_4$, at 28.4 GPa, the average ⟨Fe-O⟩ distances are 1.814(4) and 1.967(2) Å for the tetrahedral and octahedral sites, respectively, whereas within the *Bbmm* phase, at 28.4 GPa, the ⟨Fe-O⟩ distances are 1.963(2) and 2.176(2) Å for the octahedral and bicapped trigonal prism sites, respectively. Even taking into account only the six shortest Fe-O bonds within the higher coordinated site $\langle Fe-O\rangle = 2.038(3)$, which is still significantly larger than observed within the spinel phase.

Thus, we can conclude that all studied ferrite spinels undergo, at the range 25–40 GPa, a first-order structural phase transition to the postspinel $CaTi_2O_4$-type structure. This structural transition is accompanied by about 8% volume reduction. Another noticeable change in the $V(P)$ data, namely a steeper decrease of unit-cell volume with pressure increase, occurs at higher pressures, above 42, 40, and 38 GPa for $MgFe_2O_4$, $ZnFe_2O_4$, and Fe_3O_4, respectively (Fig. 5). This volume decrease is seen in $ZnFe_2O_4$ and Fe_3O_4 up to ∼60GPa, indicating a continuous increase in compressibility and furthermore showing signs of $V(P)$ stabilization between 60 and 70 GPa. Such $V(P)$ behavior suggests a significant electronic transformation taking place within the HP phase. Correspondingly, the $V(P)$ data for the postspinel phase at this pressure range could not be fit with a "standard" equation

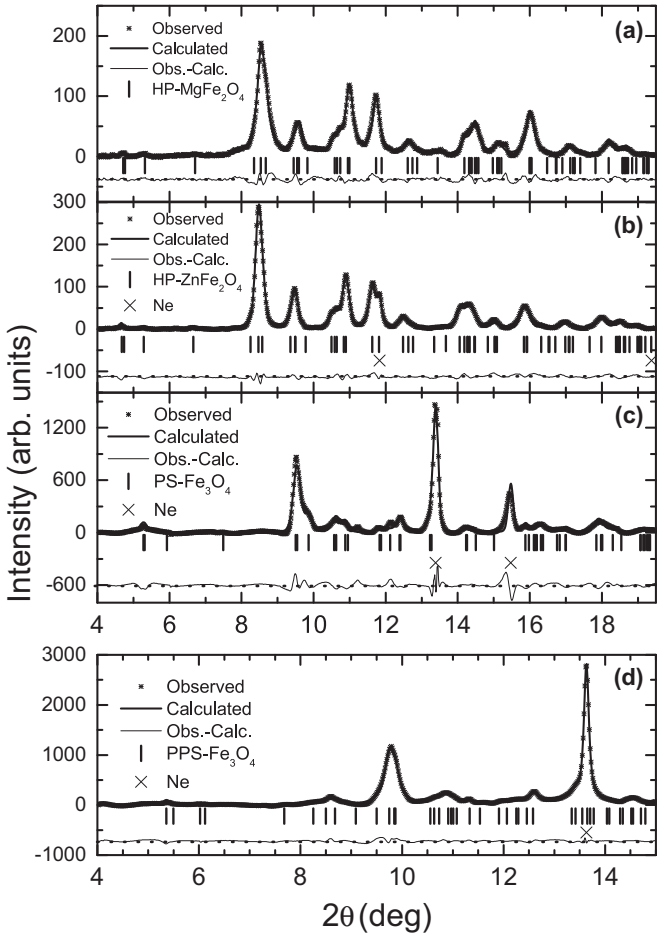

FIG. 8. Example of Rietveld refinement of the postspinel phase of (a) $MgFe_2O_4$ at 50.5(2) GPa, (b) $ZnFe_2O_4$ at 51.0(5) GPa, and (c) Fe_3O_4 at 63.6(8) GPa and RT assuming a $CaTi_2O_4$-type structure (SG *Bbmm*), and (d) F(calc) weighted (model biased) fitting of Fe_3O_4 at 79(1) GPa, assuming a *Pmma* post-postspinel type structure. Asterisks * mark the measured data, the solid line is the best fit to the data, and the dashed line shows the difference between the observed and calculated intensities (all background subtracted). Horizontal lines and X's show the expected diffraction peaks of the sample and neon, respectively. Here, $\lambda_{a,b} = 0.3738$ and $\lambda_{c,d} = 0.4152$ Å.

of state (EOS). Meanwhile, to define an EOS for the HP phase before the steeper decrease of V, one can use the data at the pressure below 40 GPa. Thus, for $ZnFe_2O_4$, the

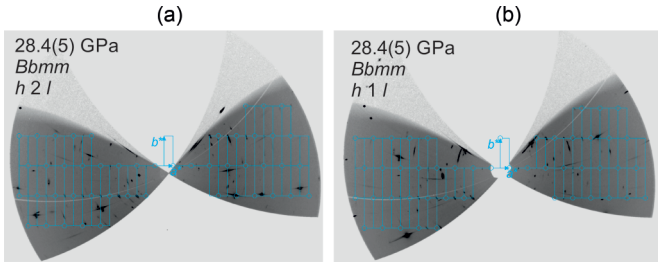

FIG. 9. Reciprocal space reconstructions of HP-Fe_3O_4 at 28.4(5) GPa corresponding to (a) h 2 l and (b) h 1 l planes, respectively. Sites on a blue lattice represent predicted positions of the reflections. Blue circles show systematic absences corresponding to B centering.

TABLE I. Details of crystal structure refinements of *Bbmm*-Fe_2MgO_4 (27.4 GPa).

Crystallographic data	Fe_2MgO_4
Crystal system	Orthorhombic
Space group	*Bbmm*
a (Å)	9.251(6)
b (Å)	9.380(4)
c (Å)	2.7583(6)
α (°)	90
β (°)	90
γ (°)	90
V(Å^3)	239.37(19)
Z	4
$F(000)$	384
θ range for data collection (°)	2.520 to 10.427
Completeness to $d = 0.8$ Å, %	0.633
Index ranges	$-8 < h < 9$ $-10 < k < 11$ $-3 < l < 3$
Reflections collected	210
Independent reflections/R_{int}	101/0.0425
Refinement method	Full matrix least squares on F^2
Data/restraints/parameters	101/1/19
Goodness of fit on F^2	1.073
Final R indices [$I > 2\sigma(I)$], R_1/wR_2	0.0412/0.0990
Type = "Periodical" R indices (all data), R_1/wR_2	0.0514/0.1104
Largest difference peak/hole (e/Å^3)	0.624/ − 0.815

data for the molar volume were fit using the second-order Birch-Murnaghan (BM2) EOS [39]. The performed fit results in $K_0 = 134(18)$ GPa and $V_0 = 571(10)$ Å^3, where K_0 and V_0 are the bulk modulus and the unit cell volume at 1 bar and 300 K, respectively. Extrapolation of the obtained EOS to higher pressures allows us to estimate a volume reduction corresponding with the proposed electronic transition. This estimation gives $\Delta V/V_0 \approx 4\%$.

It is noteworthy that, for Fe_3O_4 at pressures above 65 GPa, we observed, similar to [38], the appearance of new diffraction peaks in the XRD patterns, whose intensities start to be significant above 70 GPa (Fig. 10). The changes observed in the patterns are caused by a second structural transition to a post-postspinel phase, which is completed above 72 GPa. However, the obtained patterns differ from those observed by Ricolleau *et al.* [38], which could be related with different experimental conditions (in [38], XRD patterns were collected after annealing at temperatures up to 2300 K). In our case, the obtained patterns could be fitted well with the *Pmma* structure. A model biased F(calc) weighted refinement of the diffraction data results in a reasonable fit to the data, as evidenced in Fig. 8(d) ($w_{Rp} < 0.5\%, Rp < 0.4\%$).

Pmma is a nonisomorphic subgroup of *Bbmm*, which loses the C-centered symmetry, and the structural transition from *Bbmm* to *Pmma* belongs particularly to the order-disorder transition [40]. Correspondingly, no volume change could be expected in such a case. In agreement with this, our $V(P)$ data do not show any appreciable volume change at the transition [Fig. 5(c)]. It is noteworthy that, for Fe_3O_4, one can observe an additional kink on the $V(P)$ curve at the

TABLE II. Atomic coordinates and equivalent isotropic displacement parameters for $MgFe_2O_4$.[a]

Atom	Wyckoff site	x	y	Z	U_{eq}[b] or U_{iso}[c](Å^2)	Site occupancy
Fe1	8*f*	0.1306(2)	0.07245(18)	0.0000	0.0191(8)	0.6360(15)
Mg1	8*f*	0.1306(2)	0.07245(18)	0.0000	0.0191(8)	0.3640(15)
Fe2	4*c*	0.3815(3)	0.2500	0.0000	0.0209(9)	0.728(3)
Mg2	4c	0.3815(3)	0.2500	0.0000	0.0209(9)	0.272(3)
O1	4*b*	0.5000	0.0000	0.0000	0.021(2)	1
O2	4*c*	0.0306(13)	0.2500	0.0000	0.019(2)	1
O3	8*f*	0.2244(9)	−0.1206(7)	0.0000	0.0179(14)	1

[a]U_{eq} is defined as one third of the trace of the orthogonalized U^{ij} tensor.
[b]For metal atoms refined in anisotropic approximation.
[c]For oxygen atoms refined in isotropic approximation.

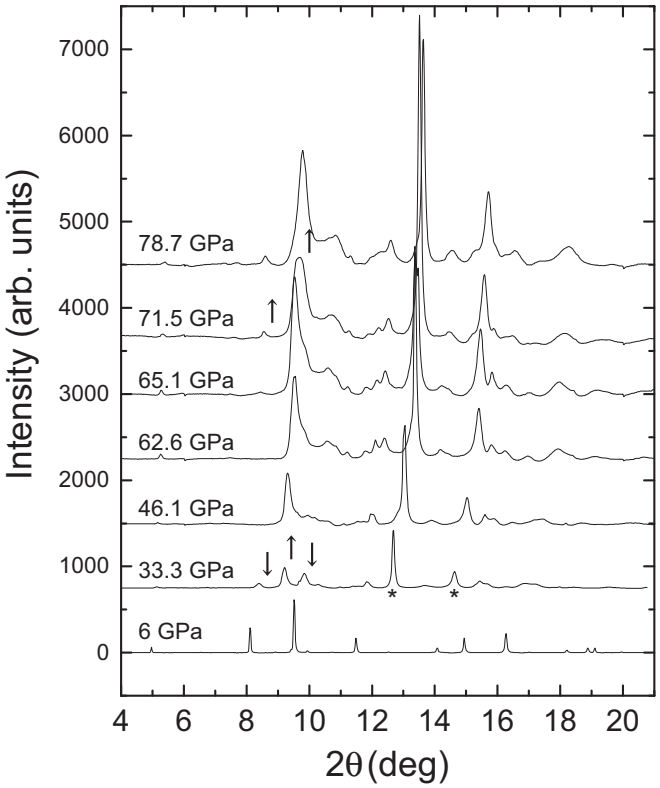

FIG. 10. Powder XRD patterns of Fe_3O_4 at various pressures during compression. At 33 GPa, * mark the Ne pressure medium peaks, ↓ mark the disappearance of the spinel phase, and ↑ mark the appearance of the *Bbmm* postspinel phase. At 71.5 GPa, ↑ mark the appearance of the post-postspinel *Pmma* phase. Here, $\lambda = 0.4152$ Å.

range 70–85 GPa characterized by a steeper volume decrease [Fig. 5(d)].

C. Resistance measurements

Here, $R(P,T)$ measurements for $MgFe_2O_4$ were carried out during compression to 81 GPa followed by decompression to ambient pressure, and for $ZnFe_2O_4$ during compression to 92 GPa. The pressure dependence of the resistance measured at RT is shown in Fig. 11. As can be seen in the spinel phase, $R(P)$ shows a minor increase with pressure increase reaching a maximum at ~25 GPa, where the postspinel phase appears. Above that, it drops continuously, demonstrating a distinctive feature at the 45–70 GPa range, namely a more rapid decrease. For $ZnFe_2O_4$, a more rapid decease of resistance was observed also in the 25–35 GPa spinel-postspinel phase coexistence range. It is noteworthy that, up to the highest pressures measured, $MgFe_2O_4$ and $ZnFe_2O_4$ remain semiconductors, showing a negative $R(T)$ slope [Fig. 11(a), inset]. At a fixed pressure, the resistivity data fairly accurately obey the relation of $lnR = lnR_0 + E/k_BT$, where k_B is the Boltzmann constant, E the electrical transport activation energy [Fig. 11(b), inset]. At the 45–85 GPa range, the value of E decreases from 0.17 to 0.11 and 0.07 eV for $MgFe_2O_4$ and $ZnFe_2O_4$, respectively. An approximation of the $E(P)$ data to highest pressures suggests a possible closing of the gap only at about 160 and 115 GPa, correspondingly.

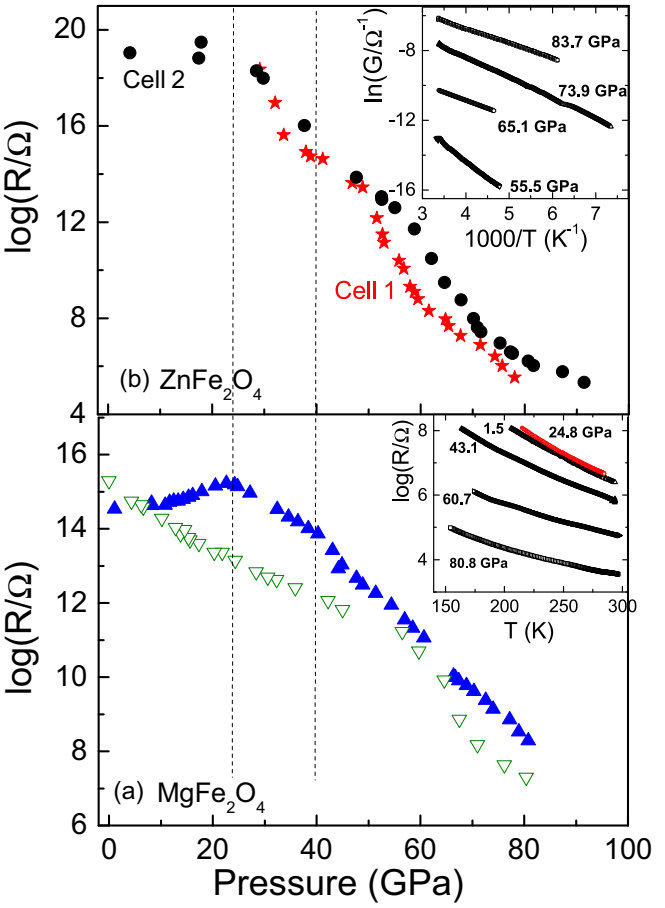

FIG. 11. The pressure dependence of the resistance of (a) $MgFe_2O_4$ and (b) $ZnFe_2O_4$ recorded at 295 K. The solid (▲) and open (▽) triangles are data points obtained during the cycles of compression and decompression, respectively, of the $MgFe_2O_4$ sample. Note the minor increase of R up to 25 GPa in the spinel phase and more rapid decrease at the range 45–70 GPa. The vertical dashed lines set the boundary of the coexistence between the spinel and postspinel phases. The inset shows $R(T)$ and conductance $G(T)$ of the samples at various pressures.

IV. DISCUSSION

Summarizing the obtained MS and XRD data, we can conclude that, for all the studied materials, a pressure-induced first-order structural phase transition takes place at the pressure range 25–40 GPa. This phase transition is manifested by the observed changes in XRD patterns and dramatic changes of the hyperfine interaction parameters. As in Fe_3O_4, the postspinel phase of MFe_2O_4 ferrites comprises two distinct Fe^{3+} sites characterized by different QS and IS values. Analysis of the powder XRD data allows assuming for the postspinel phase a $CaTi_2O_4$- or $CaMn_2O_4$-type structure. Single-crystal XRD data point at the $CaTi_2O_4$-type (*Bbmm*) as the postspinel structure in MFe_2O_4 (M = Mg,Zn,Fe) ferric spinels. Taking into account that two new MS spectral components, PS1 and PS2, are characterized by rather different QS and IS values, we can propose that the ferric ions occupy in this structure different crystallographic sites. This corresponds well with two cationic sites in the $CaTi_2O_4$-type structure, namely an

octahedral and a bicapped trigonal prism, characterized by six- and eightfold coordination polyhedra, respectively. Such different Fe^{3+} neighborhoods should result in rather different hyperfine parameters as was actually observed. It is noteworthy that the IS values for the PS1 and LP components at about 35 GPa are pretty close, while the IS value for the PS2 component is 0.065(14) and 0.084(28) mm/s higher for $ZnFe_2O_4$ and $MgFe_2O_4$, respectively, suggesting an octahedral environment, similar to the LP phase, for the PS1 component and a higher coordination number, namely bicapped trigonal prism for PS2.

In the studied ferrites, immediately following the phase transition, Fe^{3+} in both sites is in the high-spin state. However, with further pressure increase, a steeper decrease of unit-cell volume and lattice parameters is seen at the pressure range 40–70 GPa for all studied ferrites. This unusual behavior of the unit-cell volume corroborates with an appreciable change in the features of the MS spectra of $MgFe_2O_4$ and $ZnFe_2O_4$; namely, a new quadrupole-split paramagnetic component appears above ∼50 GPa, with abundance increasing sluggishly with pressure [Fig. 5(a), inset]. This new PS3 component is characterized by a significantly reduced IS value, which corresponds to an increase of the effective *s* density at the nucleus. The new quadrupole-split component can result from either (*i*) a HS-LS transition, or (*ii*) a correlation breakdown (a *Mott* transition) in which a magnetic interaction vanishes [15]. In the present case, at low temperatures, the PS3 component exhibits a smeared magnetic splitting, which is a feature of a weak magnetic interaction, a paramagnetic spin relaxation phenomenon [34]. Thus, the appearance of the features of a paramagnetic spin relaxation phenomenon at low temperatures and the absence of a corroborating insulator-to-metal transition at this pressure range allows us to conclude that the HS-LS transition takes place in the present case. Since MS observations refer to the PS1 component, as undergoing a spin crossover, we conclude that the transition to the LS state originates only on the octahedral sites. Such a transition results in shorter Fe-O distances, hence in a reduced crystal volume and lattice parameters, which were clearly observed in XRD experiments (Fig. 5). It is noteworthy that the ∼4% volume decrease, corresponding with the HS-LS transition in $ZnFe_2O_4$ $ZnFe_2O_4$ [see Fig. 5(b)], suggests about 12% decrease of the Fe^{3+} octahedral volume, which agrees well with results of previous studies [41,42]. In the case of $MgFe_2O_4$, according to single-crystal XRD data, about 64% of Fe^{3+} occupies octahedral sites; in the meantime, the abundance of the LS MS component reaches only ∼44% at 110 GPa [see Fig. 5(a), inset]. It means that, in $MgFe_2O_4$, the HS-LS transition on the octahedral sites is not finished even at such HP.

According to the XRD and MS data, the HS-LS transition is sluggish: an anomalous crystal volume behavior is observed at the range 40–70 GPa and is attributed to the interplay between normal compressibility and spin variation effect on the Fe^{3+} ionic radius. Another interesting finding is a significant decrease of the *Néel* temperature $T_N(P)$, despite an expected increase in the exchange and super-exchange interactions with density increase. This is also a consequence of the HS-LS transition on the octahedral sites, which excludes in fact nearly half of the Fe^{3+} ions from the super-exchange interaction. As a result, in both systems, T_N drops from ∼90 K at 47 GPa to ∼50 K at 80 GPa.

Thus, in contrast to other studied ferric oxides (see [15,16]), in the case of postspinel structures of $MgFe_2O_4$ and $ZnFe_2O_4$, about half of the Fe^{3+} ions remain in the HS state at least up to 110 GPa, the highest pressure achieved in this paper. Another special feature distinguishing the spinel and postspinel structures is the absence of any *first-order* pressure-induced electronic transitions typical of Fe^{3+} at these extreme conditions; namely, no Mott transition takes place as verified by the negative slope of $R(T)$ up to ∼95 GPa and the presence of magnetism. Furthermore, in $MgFe_2O_4$, no gap closure is expected up to 160 GPa. Also, no first-order HS-LS transition, typical for ferric oxides, was observed, only the sluggish spin crossover on the octahedral sites. It is noteworthy that recent studies of α-$LiFeO_2$, crystallizing in the rock salt structure with random distribution of Li and Fe ions, shows very similar features of the pressure-induced spin crossover, namely a sluggish second-order Fe^{3+} HS-LS transition, which starts at 50 GPa and is not completed even at ∼100 GPa [43]. It was proposed that the observed feature of the HS-LS transition in α-$LiFeO_2$ is caused by the random environment of Fe^{3+} ions [41]. The random environment of Fe^{3+} ions is expected also in the present ferric spinels. Hence, the presented features of the spin crossover in the studied spinels could serve as another confirmation of the effect of the nearest Fe^{3+} environment upon the transition features.

Thus, these postspinels remain, up to the highest pressures measured, semiconducting and paramagnetic with a mixed spin state: $S = 5/2$ and $S = 1/2$ for Fe^{3+} populating eight-coordination and six-coordination sites, respectively. Recent studies of Fe_2O_3, hematite [44], provide experimental and theoretical evidence for a possible site-selective *multistage* correlation breakdown. They show that, in a material with a complex crystal structure, containing transition metal cation(s) in different environments (i.e. different coordination numbers), Mott insulator-to-metal transition and collapse of magnetism does not necessarily occur simultaneously and may propagate through different crystallographic sites at different degrees of compression. In that case, a structural transition to a crystal structure with multiple crystallographic sites, with octahedral and eightfold coordinated sites, results in metallization and collapse of magnetism only in half of the Fe^{3+} (those in octahedral sites), while Fe^{3+} in the higher coordinated sites remain HS up until a second structural phase transition results in a single octahedral site for all Fe^{3+}. Our present studies of $MgFe_2O_4$ and $ZnFe_2O_4$ postspinels demonstrate similar features also for a HS-LS transition. Such a site-selective spin transition was recently discovered in $(Mg,Fe)(Si,Fe)O_3$ perovskite, where according to both experiments [45] and DFT + U calculations [46], Fe^{3+} in octahedral sites undergoes the transition to low-spin in the range of 40–70 GPa, while Fe^{3+} in dodecahedral sites remains high-spin.

Similar conclusions could be reached also for Fe_3O_4, magnetite. However, in the case of Fe_3O_4, where $Mg^{2+}(Zn^{2+})$ is replaced by Fe^{2+}, the observed electronic transformation is even more complicated. Indeed, the performed low-temperature MS studies of magnetite show an evolution of the MS spectra at the pressure range 40–60 GPa, which is similar to the other studied ferrites. As was mentioned above, Fe_3O_4 postspinel phase,

at its appearance, is characterized by three equally abundant HS Fe components [Fe^{2+}, Fe^{3+}(I), Fe^{3+}(II)] [11]. Taking into account the significantly lower IS value obtained for the Fe^{3+}(I) component, compared to the Fe^{3+}(II) component (see Fig. 6), one can suggest an octahedral environment for the Fe^{3+}(I) sites and bicapped trigonal prism for the Fe^{3+}(II). At pressures above 40 GPa, similar to $MgFe_2O_4$ and $ZnFe_2O_4$, a new quadrupole-split component $Fe^{3+}(I)_{nm}$, characterized by a significantly reduced IS value, emerges at the center of the spectra, gradually replacing the Fe^{3+}(I) component (Fig. 6). Correspondingly, T_N drops to 160 K at 82 GPa. Coinciding with the onset of this MS component, the steeper decrease of unit-cell volume is observed above 38 GPa followed by the $V(P)$ stabilization above 57 GPa. This suggests that, similar to $MgFe_2O_4$ and $ZnFe_2O_4$, a second-order HS-LS transition takes place on the octahedral Fe^{3+}(I) sites. In Fe_3O_4, this electronic transition is followed by the structural transition from *Bbmm* to *Pmma* structure, which could be considered as the order-disorder transition [40]. In a similar transition in Fe_2TiO_4 [40], the octahedral cationic sites of the *Bbmm* structure are split into two crystallographic nonequivalent sites in post-postspinel *Pmma*, where Fe^{2+} and Ti^{4+} are ordered on the sixfold coordination sites $4i$ and $4j$, respectively. In the case of Fe_3O_4, the low-spin Fe^{3+} ion, characterized by an extremely small ionic radius compared to HS Fe^{2+}, plays the role of Ti^{4+}, initiating obviously the transition to the *Pmma* structure, where LS Fe^{3+} and HS Fe^{2+} are ordered on the sixfold coordination sites similar to Fe_2TiO_4.

It is noteworthy that, in contrast to $MgFe_2O_4$ and $ZnFe_2O_4$, where the Fe^{3+} HS-LS transition on the octahedral sites does not result in a closure of the insulating gap, in the case of Fe_3O_4, one can observe a clear trend towards a gap closure above 50 GPa [11]. Upon its inception, at ~25 GPa, the HP phase of Fe_3O_4 is a semiconductor with relatively strong carrier localization [11], but corroborating with the second-order HS-LS transition of ferric ions on the octahedral sites, an incipient semimetal behavior is observed, characterized by rather complicated $R(T)$ features (see Fig. 12). With further pressure increase, an onset of the new nonsplit $Fe^{2+}{}_{nm}$ component in low-temperature MS spectra is observed around 70 GPa (Fig. 6) following the structural transition to *Pmma* phase above 65 GPa and corroborating with a steeper decrease of unit-cell volume at the pressure range 70–85 GPa. This signifies further propagation of the gradual collapse of magnetism corroborating with a continuous sluggish metallization process, which results in a distinct metallic behavior above 90 GPa (Fig. 12). We note that a recent study of the electrical transport properties of Fe_3O_4 by Muramatsu *et al.* [47], despite qualitative agreement with our data, did not detect an onset of positive $R(T)$ slope up to 98 GPa. In this paper, such a slope occurs at $P \geqslant 99$ GPa. What is clear from their study is, similar to this paper, the tendency towards gap closure above 60 GPa, with the resistance changing by a factor of ~2 from RT down to a few Kelvin above 64 GPa, signifying that the sample is in fact no longer semiconducting. The difference between the results of both of these studies could be related to the sensitivity of the appearance of the metallic phase to stress conditions (e.g. Daphne oil vs Al_2O_3/NaCl pressure medium), sample stoichiometry (see sample synthesis details in [48]), and the details of the measurement technique (e.g. contact resistance, direct contact between sample and diamond-anvil, maximum applied electric current). It is noteworthy that, in He pressure medium, the transformation HS $Fe^{2+} \rightarrow Fe^{2+}{}_{nm}$ is completed already at about 85 GPa, and furthermore, no appreciable change of the MS spectra is observed, while in the N_2 pressure medium, the transition is not completed even at 120 GPa. The lack of any sign of a magnetic interaction for $Fe^{2+}{}_{nm}$ and $Fe^{3+}(I)_{nm}$ components above 84 GPa and down to 2.4 K (Fig. 7) prompted us to conclude that these components emanate not from a paramagnetic, but rather from a nonmagnetic state [49]. All these features, namely the loss of the magnetic interactions corroborating with the onset of metallic state, are typical features of the correlation breakdown in strongly correlated systems [15,50,51]. However, in the case of Fe_3O_4, one can see that the correlation breakdown takes place only in the octahedral sublattice, while a third of the iron cations, namely Fe^{3+}(II) sites, remain in the HS state. As it was mentioned above, a similar site-selective Mott transition was observed recently in Fe_2O_3, where a partial collapse of magnetism concurrent with an insulator-to-metal transition takes place around 50 GPa, while a complete collapse of magnetism and correlation breakdown was observed only at ~70 GPa. In Fe_3O_4, the process is even more complicated. The second-order HS-LS transition on the Fe^{3+} octahedral sites, starting around 40 GPa, corroborates with a clear trend to gap closure and formation of a semimetal state above 50 GPa. Above 70 GPa, a sluggish metallization process also is further observed, corroborating with the onset of the nonmagnetic Fe^{2+} component. This very sluggish metallization process, corroborating with the gradual collapse of magnetism, presumably only on the octahedral sites, is a characteristic feature of the multistage correlation breakdown at the present case. However, even at 120 GPa, the Mott transition in Fe_3O_4 is not completed yet since Fe^{3+}(II) still remain in the HS state. It is noteworthy that the comparison with two other studied spinels allows us to propose a crucial role of the substitution of Mg/Zn in the octahedral sites by Fe^{2+} ions, which results in

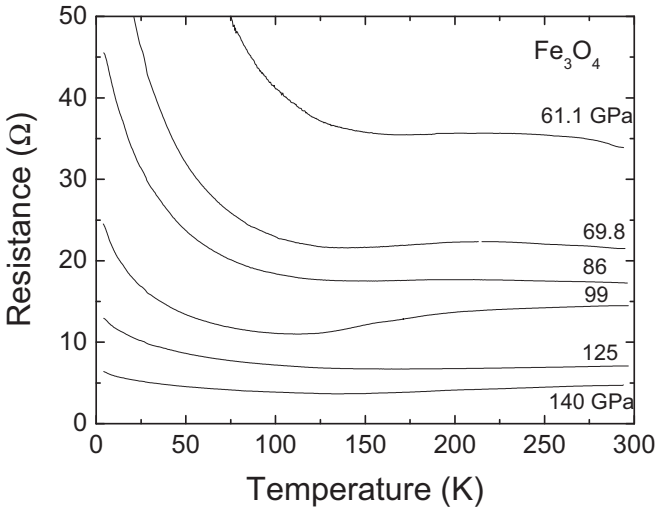

FIG. 12. The temperature dependence of the resistance of Fe_3O_4 at various pressures (part of these data were published previously in [14]). An incipient semimetal behavior is observed above 60 GPa followed by a sluggish metallization above 86 GPa.

the closure of the gap at relatively LPs. In two other materials ($MgFe_2O_4$ and $ZnFe_2O_4$), the gap closure is expected only above 115 GPa, and obviously, because of the complex crystal structure, containing Fe^{3+} in different environments, this will be only the first stage of the multistage process. It is noteworthy that a recent publication of Rahman *et al.* [52] claims a spin crossover and the onset of the Mott insulator-metal transition (IMT) in the mixed $Zn_{0.2}Mg_{0.8}Fe_2O_4$ spinel, corroborating with the transition to a postspinel phase around 20 GPa. This claim was based on the disappearance of all the Raman modes above 33 GPa and the absence of the resistivity variation at the temperature range 300–420 K. However, taking into account the results obtained in this paper for the pure $MgFe_2O_4$ and $ZnFe_2O_4$ spinels, the claimed IMT and a collapse of Fe^{3+} magnetic moments at such relatively LPs raises many questions and requires, obviously, further verification (for details, see Fig. S2 in the Supplemental Material [36]).

V. CONCLUSIONS

In conclusion, our studies reveal for all studied ferric spinels, MFe_2O_4 (M = Mg,Zn,Fe), at the pressure range 25–40 GPa, an irreversible first-order structural transition to the postspinel $CaTi_2O_4$-type structure. The postspinel phase is characterized by a partial inversion of the orthorhombic *Bbmm* structure and associated Fe $\leftrightarrow$ M site exchange, where about half of Fe^{3+} enters eightfold coordinated polyhedral sites. In all studied postspinel phases, a second-order HS-LS transition is observed on the octahedral Fe^{3+} sites at around the range of 40–60 GPa, while Fe^{3+} cations occupying bicapped trigonal prism sites remain in the HS state. The observed features of the pressure-induced HS-LS transition in the studied spinels serve as further evidence of the effect of the nearest Fe^{3+} environment upon the spin crossover features [43].

The HS-LS transition is accompanied by an appreciable resistance decrease, but $MgFe_2O_4$ and $ZnFe_2O_4$ remain semiconducting up to ~90 GPa, and the gap closure is expected only above ~115 GPa. Contrarily, in the case of Fe_3O_4, the sluggish HS-LS transition on the Fe^{3+} octahedral sites corroborates with a clear trend to a gap closure and formation of a semimetal state above 50 GPa. Above 70 GPa, a gradual collapse of magnetism corroborating with a sluggish metallization process further extends capturing also Fe^{2+} sites, while about half of Fe^{3+} sites still remain in the HS state. These electronic transformations in Fe_3O_4 coincide with another structural phase transition to the post-postspinel *Pmma* structure. All these features are characteristics of the multistage correlation breakdown process, confirming the concept of a site-selective Mott transition proposed recently in [44].

ACKNOWLEDGMENTS

A few of the SXRD data were collected at the ID-09 beamline of the ESRF, Grenoble, France. We are grateful to Michael Hanfland at the ESRF for providing assistance in using beamline ID-09. We thank A. Melchior and R. Arielly for assisting with the powder XRD measurements. We thank S. Layek and M. Shulman for assisting with the SMS measurements. We thank A. Motil for his assistance with analysis of related XRD data. We are grateful to Ulf Hålenius (Swedish Museum of Natural History, Stockholm, Sweden) for providing the single crystal of $MgFe_2O_4$. This research was supported by the Israeli Science Foundation under Grant No. 1189/14. The authors are grateful to A. Kurnosov for his assistance with the Raman spectroscopy measurements.

[1] K. E. Sickafus, J. M. Wills, and N. W. Grimes, J. Am. Ceram. Soc. **82**, 3279 (1999).
[2] H. Kawai, M. Nagata, H. Kageyama, H. Tukamoto, and A. R. West, Electrochim. Acta **45**, 315 (1999).
[3] D. C. Johnston, J. Low Temp. Physics **25**, 145 (1976).
[4] C. P. Sun, Y. F. Huang, S. T. Tsai, C. L. Huang, and H. D. Yang, Phys. B (Amsterdam, Neth.) **378**, 395 (2006).
[5] N. Grimes, Phys. Technol., **6**, 22 (1975).
[6] L. W. Finger, R. M. Hazen, and A. M. Hofmeister, Phys. Chem. Miner. **13**, 215 (1986).
[7] T. Irifune, K. Fujino, and E. Ohtani, Nature **349**, 409 (1991).
[8] N. Funamori, R. Jeanloz, J. H. Nguyen, A. Kavner, W. A. Caldwell, K. Fujino, N. Miyajima, T. Shinmei, and N. Tomioka, J Geophys. Res. **103**, 20813 (1998).
[9] D. Levy, A. Pavese, and M. Hanfland, Phys. Chem. Miner. **27**, 638 (2000).
[10] D. Andrault and N. Bolfan-Casanova, Phys. Chem. Miner. **28**, 211 (2001).
[11] W. M. Xu, G. Yu. Machavariani, G. K. Rozenberg, and M. P. Pasternak, Phys. Rev. B **70**, 174106 (2004).
[12] Y. Fei, D. J. Frost, H. K. Mao, C. T. Prewitt, and D. Hausermann, Am. Mineral. **84**, 203 (1999).
[13] C. Haavik, S. Stølen, H. Fjellvåg, M. Hanfland, and D. Häusermann, Am. Mineral. **85**, 514 (2000).
[14] L. S. Dubrovinsky, N. A. Dubrovinskaia, C. McCammon, G. Kh. Rozenberg, R. Ahuja, J. M. Osorio-Guillen, V. Dmitriev, H.-P. Weber, T. L. Bihan, and B. Johansson, J. Phys.: Condens. Matter **15**, 7697 (2003).
[15] G. Kh. Rozenberg, W. Xu, and M. P. Pasternak, Z. Kristallogr. - Cryst. Mater. **229**, 210 (2014).
[16] A. Friedrich, B. Winkler, W. Morgenroth, J. Ruiz-Fuertesand, M. Koch-Müller, D. Rhede, and V. Milman, Phys. Rev. B **90**, 094105 (2014).
[17] E. Greenberg, G. K. Rozenberg, W. Xu, R. Arielly, M. P. Pasternak, A. Melchior, G. Garbarino, and L. S. Dubrovinsky, High Press. Res. **29**, 764 (2009).
[18] G. Yu. Machavariani, M. P. Pasternak, G. R. Hearne, and G. K. Rozenberg, Rev. Sci. Instrum. **69**, 1423 (1998).
[19] R. Letoullec, J. P. Pinceaux, and P. Loubeyre, High Pressure Res. **1**, 77 (1988).
[20] R. A. Forman, G. J. Piermarini, J. D. Barnett, and S. Block, Science **21**, 284 (1972).
[21] H. K. Mao, P. M. Bell, J. W. Shaner, and D. J. Steinberg, J. Appl. Phys. **49**, 3276 (1978).
[22] H. K. Mao, J. Xu, and P. M. Bell, J. Geophys. Res. **91**, 4673 (1986).
[23] S. H. Shim, T. S. Duffy, and T. Kenichi, Earth Planet. Sci. Lett. **203**, 729 (2002).

[24] V. Potapkin, A. I. Chumakov, G. V. Smirnov, J.-P. Celse, R. Rüffer, C. McCammon, and L. Dubrovinsky, J. Synchrotron Radiat. **19**, 559 (2012).
[25] C. Prescher, C. McCammon, and L. Dubrovinsky, J. Appl. Crystallogr. **45**, 329 (2012).
[26] A. P. Hammersley, ESRF Internal Report, ESRF97HA02T (1997).
[27] A. P. Hammersley, S. O. Svensson, M. Hanfland, A. N. Fitch, and D. Häusermann, High Press. Res. **14**, 235 (1996).
[28] C. Prescher and V. B. Prakapenka, High Press. Res. **35**, 223 (2015).
[29] A. C. Larson and R. B. Von Dreele, General Structure Analysis System (GSAS), Los Alamos National Laboratory Report LAUR 86-748 (1994).
[30] B. H. Toby, J Appl. Crystallogr. **34**, 210 (2001).
[31] H.-P. Liermann, Z. Konopkova, W. Morgenroth, K. Glazyrin, J. Bednarcik, E. E. McBride, S. Petitgirard, J. T. Delitz, M. Wendt, Y. Bican, A. Ehnes, I. Schwark, A. Rothkirch, M. Tischer, J. Heuer, H. Schulte-Schrepping, T. Kracht, and H. Franz, J. Synchrotron Radiat. **22**, 908 (2015).
[32] CrysAlisPro Software system. Version 1.171.37.28. Oxford: Agilent Technologies UK Ltd., 2013.
[33] G. M. Sheldrick, Acta Crystallogr. A **64**, 112 (2008).
[34] W. Schiessl, W. Potzel, H. Karzel, M. Steiner, G. M. Kalvius, A. Martin, M. K. Krause, I. Halevy, J. Gal, W. Schafer, G. Will, M. Hillberg, and R. Wappling, Phys. Rev. B **53**, 9143 (1996).
[35] W. M. Xu, O. Naaman, G. K. Rozenberg, M. P. Pasternak, and R. D. Taylor, Phys. Rev. B **64**, 094411 (2001).
[36] See Supplemental Material at http://link.aps.org/supplemental/10.1103/PhysRevB.95.195150 for Raman spectroscopy data and further plots of selected MS spectra, and tables of single-crystal data for Fe_3O_4.
[37] For Fe_3O_4 the unit-cell volume within the $CaTi_2O_4$ type structure was determined by indexation of the peaks 002, 024, 130, and 131 (using the *Cmcm* settting) for most of the pressure range, since the multiple pressure-induced transitions resulted in significant broadening of most peaks, making it difficult to obtain a reliable and consistent fit to the patterns.
[38] A. Ricolleau and Y. Fei, Am. Mineral. **101**, 719 (2016).
[39] O. L. Anderson, *Equations of State of Solids for Geophysics and Ceramic Science* (Oxford University Press, Oxford, 1995).
[40] T. Yamanaka, Y. Nakamoto, A. Kyono, Y. Meng, S. Kharlamova, V. V. Struzhkin, and H. K. Mao, Am. Mineral. **98**, 736 (2013).
[41] M. Merlini, M. Hanfland, M. Gemmi, S. Huotari, L. Simonelli, and P. Strobel, Am. Mineral. **95**, 200 (2010).
[42] E. Greenberg, G. K. Rozenberg, W. Xu, M. P. Pasternak, C. McCammon, K. Glazyrin, and L. S. Dubrovinsky, Phys. Rev. B **88**, 214109 (2013).
[43] S. Layek, E. Greenberg, W. Xu, G. K. Rozenberg, M. P. Pasternak, J.-P. Itié, and D. G. Merkel, Phys. Rev. B **94**, 125129 (2016).
[44] E. Greenberg, I. Leonov, S. Layek, Z. Konopkova, M. P. Pasternak, L. Dubrovinsky, R. Jeanloz, I. A. Abrikosov, and G. K. Rozenberg (unpublished).
[45] K. Catalli, S.-H. Shim, V. B. Prakapenka, J. Zhao, W. Sturhahn, P. Chow, Y. Xiao, H. Liu, H. Cynn, and W. J. Evans, Earth Planet. Sc. Lett. **289**, 68 (2010).
[46] H. Hsu, P. Blaha, M. Cococcioni, and R. Wentzcovitch, Phys. Rev. Lett. **106**, 118501 (2011).
[47] T. Muramatsu, L. V. Gasparov, H. Berger, R. J. Hemley, and V. V. Struzhkin, J. Appl. Phys. **119**, 135903 (2016).
[48] G. Kh. Rozenberg, G. R. Hearne, M. P. Pasternak, P. A. Metcalf, and J. M. Honig, Phys. Rev. B **53**, 6482 (1996).
[49] Here, nonmagnetic means absence of any signs of magnetic correlations down to lowest measured temperature.
[50] N. F. Mott, *Metal-Insulator Transitions* (Taylor and Francis, London, 1990).
[51] M. Imada, A. Fujimori, and Y. Tokura, Rev. Mod. Phys. **70**, 1039 (1998).
[52] S. Rahman, S. Samanta, D. Errandonea, Sh. Yan, Ke Yang, J. Lu, and L. Wang, Phys. Rev. B **95**, 024107 (2017).